

From shear stress to wall pressure spectra: a semi-analytical approach to account for mean pressure gradients in turbulent boundary layers

Simon L. Prigent*  and Christophe Bailly 

Univ Lyon, Ecole Centrale de Lyon, CNRS, Univ Claude Bernard Lyon 1, INSA Lyon, Laboratoire de Mécanique des Fluides et d'Acoustique, UMR5509, 69130 Ecully, France

Received 14 February 2022, Accepted 12 August 2022

Abstract – This study offers a semi-analytical means to compute the wall pressure spectra beneath a turbulent boundary layer depending only on the latter's Kármán number and dimensionless pressure gradient. By inclusion of the total mean shear profiles in a mixing length model, the velocity profiles can be reconstructed under adverse, zero- and favourable pressure gradients. These profiles serve as input to existing models of the wall pressure spectra and thus remove the need for experimental or numerical data. The modelled frequency spectra fairly estimate the level of the measured ones. The three typical regions of those spectra are recovered, although the overlap one is shorter than with experimental data, and the trends of pressure gradients effects are also observed. The wavenumber representation shows the effect of pressure gradients on the convective ridge structure as its aspect ratio increases from adverse to favourable ones. The same variation is observed in experimental data, and although the absolute values of the aspect ratios do not match, qualitative observations can be made.

Keywords: Wall pressure spectra, Pressure gradient, Turbulent boundary layer, Analytical model

1 Introduction

The study of wall pressure fluctuations beneath a turbulent boundary layer has drawn the attention of researchers for decades [1, 2] due to their importance in a wide range of applications dealing with vibro-acoustics or aero-acoustics. There are still open questions and ongoing research for which the context has been discussed by the authors of studies on the experimental [3] or numerical [4, 5] characterisation of their wavenumber–frequency spectra, and the ability to account for pressure gradients [5, 6] for instance. There are different ways of modelling the spectra of such fluctuations, two broad categories being semi-empirical models and analytical ones.

Semi-empirical models are rather common in the literature, the one proposed by Goody [7] being perhaps the prime example. Subsequent studies have modified it to account for various parameters, such as the free stream pressure gradient (e.g. Rozenberg et al. [8]) and all share the same structure with coefficients adapted to the specifications of each application, as discussed by Lee [9].

The approach followed in the present work is somewhat different as it is based on a physical equation. Statistical modelling of the wall pressure spectra beneath a turbulent boundary layer, based on the work of Kraichnan [10], uses

the Poisson equation to relate pressure and velocity statistics:

$$\frac{1}{\rho} \nabla^2 p = \underbrace{-2 \frac{\partial u'_i}{\partial x_i} \frac{\partial U_i}{\partial x_j}}_{(a)} - \underbrace{\frac{\partial^2}{\partial x_i \partial x_j} (u'_i u'_j - \overline{u'_i u'_j})}_{(b)}, \quad (1)$$

where p denotes pressure fluctuations, and U_i and u'_i the mean and fluctuating velocities for the i th component. The overbar is associated with the statistical average. The wavenumber–frequency transform of the pressure fluctuations at the wall can then be expressed as a weighted integral of a source term across the boundary layer. The turbulence-turbulence term (b) is usually left aside, since its contribution is often much smaller than the turbulence-mean shear one (a) [11] and it requires tedious numerical integrations to be computed [11, 12]. The wall pressure spectrum involves the expected value of the product of the wavenumber–frequency transform by its complex conjugate, and a double integral along the wall normal direction must be determined. Two approaches have been used in previous studies to deal with this difficulty and have led to the two formulations of statistical models that shall be discussed hereafter. In the first approach, leading to the so called tno-Blake model [13, 14], the velocity fluctuations in the turbulent boundary layer are assumed to be uncorrelated over the wall normal direction which reduces the

*Corresponding author: simon.prigent@ec-lyon.fr

expression to only one integral. However, a vertical integral scale is used as a correcting factor to account for the non-physicality of this assumption. This results in the following formulation for the wall pressure spectrum Φ_{pp} :

$$\begin{aligned} \Phi_{pp}^{mo}(k_1, k_3, \omega) &\simeq 8\rho^2 \int_0^\infty \left(\frac{dU_1}{dx_2}\right)^2 L_2 \phi_{22}(k_1, r_2 = 0, k_3) \\ &\times \frac{k_1^2}{k_1^2 + k_3^2} e^{-2\sqrt{k_1^2 + k_3^2}x_2} \phi_m(\omega, \mathbf{k}) dx_2, \end{aligned} \quad (2)$$

where k_1 and k_3 are the streamwise and transverse wavenumbers, dU_1/dx_2 is the mean shear, L_2 represents a vertical integral length scale, ϕ_{22} is the spectrum of the wall-normal velocity fluctuations, r_2 the wall-normal separation and ω the angular frequency. Note that ϕ_{22} is expressed in the wavenumber space only for the two directions parallel to the wall. The filter ϕ_m represents the dispersion relation for the frequency dependence. The second approach, followed by Lysak in a study of turbulent pipe flows [15], uses a Fourier pair to remove one of the integral, which requires that the velocity spectrum be expressed in the wavenumber space for all three directions. One notices that the inherent assumption of flow homogeneity is at least questionable in a boundary layer. The outcome of this approach is

$$\begin{aligned} \Phi_{pp}^{Lys}(k_1, k_3, \omega) &\simeq 8\pi\rho^2 \int_0^\infty \left(\frac{dU_1}{dx_2}\right)^2 \phi_{22}(k_1, k_2 = 0, k_3) \\ &\times \frac{k_1^2}{k_1^2 + k_3^2} e^{-2\sqrt{k_1^2 + k_3^2}x_2} \phi_m(\omega, \mathbf{k}) dx_2. \end{aligned} \quad (3)$$

Lysak uses $\phi_m(\omega, \mathbf{k}) = \delta(\omega - U_1 k_1)$ which corresponds to a frozen turbulence hypothesis with a convection by the local mean velocity.

Recent studies have looked into the modelisation of the velocity fluctuations, corresponding to the spectra $\phi_{22}(k_1, r_2 = 0, k_3)$ and $\phi_{22}(k_1, k_2 = 0, k_3)$ in the previous equations. Grasso et al. [11] have summarized the discussions and provided further details on the choice of the models themselves. They have compared different models to direct numerical simulations. From their results it appears that the standard von Kármán model is satisfactory, but improvements in modelling the correlations can be brought by the use of higher order models of its generalised form corresponding to the Liepman one or the rapid distortion theory. In addition, Morilhat et al. [16] have recently conducted measurements of the wall-normal velocity correlation without pressure gradient and reported that the von Kármán formulation offered a good approximation. These considerations were based on isotropic models and indeed Grasso et al. [11] mentioned that anisotropy would be of importance only in the innermost part of the boundary layer. However, several studies have looked into taking into account the anisotropy or inhomogeneity of the flow. Bertagnolio, Fischer, and Zhu [17] used the tno-Blake formulation and accounted for anisotropy in the flow by the use of stretching factors which enable the anisotropic spectrum to be explicitly linked to an isotropic one, as

previously explained by Lynch, Blake, and Mueller [18]. These stretching factors were based on the mean pressure gradient [17] which had the disadvantage to fail in zero-pressure gradient flows. Slama, Leblond, and Sagau [4] followed a different approach and worked in the space-time domain to include both turbulence-mean shear and turbulence-turbulence interaction terms, from equation (1). Their model accounted for anisotropy with a model for the velocity correlations describing not only the stretching but also the inclination of their shape, which was calibrated with DNS results on a zero-pressure gradient flow. Recently, Jaiswal et al. [12] focused on computing the wall pressure spectra from velocity fluctuations data, acquired from particle image velocimetry. The authors [12] concluded that isotropic models could be used with a fair degree of accuracy provided that inhomogeneity was accounted for, since the blocking effect due to the wall was found significant in the correlation functions. The authors redefined the two-point correlation length scale as the algebraic mean of the standard one computed at each point. Further, they showed that the use of Λ_{22}^2 as the length scale of reference for the velocity spectra model, instead of Λ_{11}^1 as done by Grasso et al. [11] lead to more accurate results. While this discussion is important and sheds light on the limits of potential assumptions and derivations that shall be carried out later in this study, most of the data is not available within the frame of our study since the goal is to work with as few parameters as possible, and not to rely on experimental nor numerical data.

It should be noted that Morilhat et al. [16] measured the convection velocity from the velocity fluctuations' correlation and found it was very close to the local mean velocity. This latter result supports the assumption of frozen turbulence in defining ϕ_m .

As pointed out by Grasso et al. [11], most of the studies using or building upon the tno-Blake approach [19, 20] use experimental or CFD data for the velocity profiles, which is the last term to compute after having discussed the velocity spectra and correlation scales. For turbulent boundary layers in a pipe flow, Lysak [15] had the idea to reconstruct the mean velocity profile from a mixing length model. However, that study assumed a constant total mean shear and did not account for mean pressure gradients. The goal of the present study is thus to extend the work of Lysak [15] and present a methodology to compute the mean velocity profiles that accounts for the effect of mean pressure gradients, solely based on the Kármán number and the normalised pressure gradient. This methodology shall also provide a length scale to inform the chosen velocity spectra model. Finally, using these modelled profiles and a velocity spectra model, both Lysak and tno-Blake formalisms can be used to compute the wall pressure spectra.

2 Mixing length model to rebuild velocity profiles

The mean velocity is governed by the following equations

$$\begin{cases} \frac{\partial \bar{U}_1}{\partial x_1} + \frac{\partial \bar{U}_2}{\partial x_2} = 0, \\ \rho \left(\bar{U}_1 \frac{\partial \bar{U}_1}{\partial x_1} + \bar{U}_2 \frac{\partial \bar{U}_1}{\partial x_2} \right) = -\frac{dP_e}{dx_1} + \frac{\partial \bar{\tau}_t}{\partial x_2}, \end{cases}$$

where $\bar{\tau}_t$ is the total shear stress, defined as

$$\bar{\tau}_t = -\rho \overline{u'_1 u'_2} + \mu \frac{\partial \bar{U}_1}{\partial x_2} = (\mu + \mu_t) \frac{\partial \bar{U}_1}{\partial x_2},$$

with ρ the density, μ and μ_t the molecular and turbulent dynamic viscosities respectively and P_e the external mean pressure to the boundary layer.

By integration of the momentum equation in the direction normal to the wall, one gets

$$\bar{\tau}_t = \tau_w + \underbrace{\int_0^{x_2} \rho \left(\bar{U}_1 \frac{\partial \bar{U}_1}{\partial x_1} + \bar{U}_2 \frac{\partial \bar{U}_1}{\partial x_2} \right) dx_2}_{(a)} + \frac{dP_e}{dx_1} x_2, \quad (4)$$

where the term (a) is expected to be very small near the wall. By introducing a mixing length l_m to build a zero-equation eddy viscosity model, the mean velocity profile can be calculated from

$$\frac{\partial \bar{U}_1^+}{\partial x_2^+} = \frac{2\bar{\tau}_t^+}{1 + \sqrt{1 + (2l_m^+)^2 \bar{\tau}_t^+}}. \quad (5)$$

The superscript $+$ denotes the wall unit normalisation, such that $\bar{U}_1^+ = \bar{U}_1/u_\tau$, $\bar{\tau}_t^+ = \bar{\tau}_t/\tau_w$ and $x_2^+ = x_2 u_\tau/\nu$, where u_τ is the friction velocity and ν the kinematic viscosity.

In Bailly and Comte-Bellot [21], the total shear stress is approximated by a linear relation for a zero-pressure-gradient boundary layer using equation (4)

$$\bar{\tau}_t^+ \simeq 1 - \frac{x_2^+}{\text{Re}^+},$$

with $x_2^+/\text{Re}^+ = x_2/\delta$. This expression can be improved as proposed by Thomas and Hasani [22] and discussed in White [23], the total shear stress $\bar{\tau}_t$ is then provided by

$$\bar{\tau}_t^+ \simeq 1 - 3 \left(\frac{x_2^+}{\text{Re}^+} \right)^2 + 2 \left(\frac{x_2^+}{\text{Re}^+} \right)^3. \quad (6)$$

Note that these expressions can be generalised in the presence of a mean pressure gradient, that is $dP_e/dx_1 \neq 0$. A first dimensionless parameter based on the boundary layer thickness δ is defined as

$$\beta_P \equiv \frac{\delta}{\tau_w} \frac{dP_e}{dx_1}.$$

By also introducing the dimensionless variable $\xi_2 \equiv x_2/\delta = x_2^+/\text{Re}^+$, the profile of the total mean shear stress is now approximated by Thomas and Hasani [22]

$$\bar{\tau}_t^+ \simeq 1 + \beta_P \xi_2 - (3 + 2\beta_P) \xi_2^2 + (2 + \beta_P) \xi_2^3. \quad (7)$$

When $\beta_P = 0$, equation (6) is retrieved. The same asymptotic behaviour is found from equations (4) to (7) with the

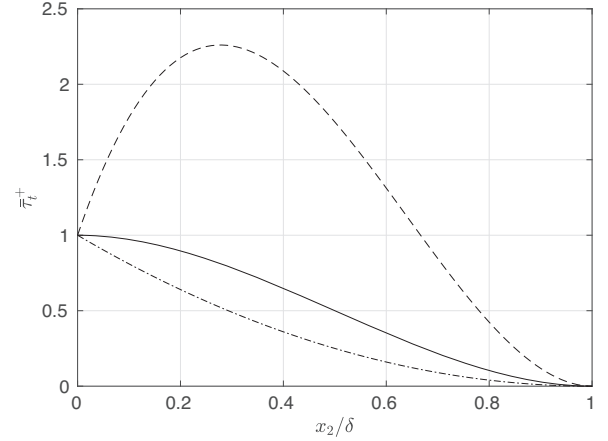


Figure 1. Profiles of $\bar{\tau}_t^+$ for (---) $\beta_P = 10$, (—) $\beta_P = 0$ and (-·-) $\beta_P = -2$.

inner part of the mean shear stress profile described by $\bar{\tau}_t^+ = 1 + \beta_P \xi_2$ when $\xi_2 \ll 1$, in the viscous sublayer. The profile verifies the constraints $\bar{\tau}_t^+ = 1$ at the wall, and $\bar{\tau}_t^+ = 0$ and $d\bar{\tau}_t^+/d\xi_2 = 0$ for $\xi_2 = 1$, that is at the edge of the boundary layer. They are plotted in Figure 1 as an illustration.

The van Driest expression [21, 24] is classically used to determine l_m for a boundary layer. The model considered in this study contains the inner part of the boundary layer and an outer part to describe the wake law associated with a constant turbulent viscosity, with a smooth transition between the two regions. Following [23, 25, 26], equations (5) and (6) are integrated with

$$\begin{cases} l_{m \text{ inner}}^+ = \kappa x_2^+ \sqrt{\bar{\tau}_t^+} (1 - e^{-\frac{x_2^+}{A_0}}), \\ l_{m \text{ outer}}^+ = A_w \text{Re}^+, \\ l_m^+ = l_{m \text{ outer}}^+ \tanh \left(\frac{l_{m \text{ inner}}^+}{l_{m \text{ outer}}^+} \right). \end{cases}$$

A smooth transition is obtained using the hyperbolic tangent function [27]. The numerical values of the constants are $A_0 = 26$ for the van Driest constant and $A_w = 0.085$ to compute l_m^+ in the outer region, as recommended in the literature.

There is a difficulty for favourable pressure-gradient boundary layers ($\beta_P < 0$), since the formulation of Thomas and Hasani [22] leads to

$$\frac{d\bar{\tau}_t^+}{d\xi_2} = \beta_P - 2(3 + 2\beta_P)\xi_2 + 3(2 + \beta_P)\xi_2^2,$$

which indicates the presence of the two local extrema

$$\xi_2^+ = 1 \quad \text{and} \quad \xi_2^- = \frac{\beta_P}{3(2 + \beta_P)},$$

where $\xi_2^- \in [0, 1]$ for $\beta_P \leq -3$. In that case $\bar{\tau}_t^+$ takes negative values, which is not physical for accelerated boundary layers.

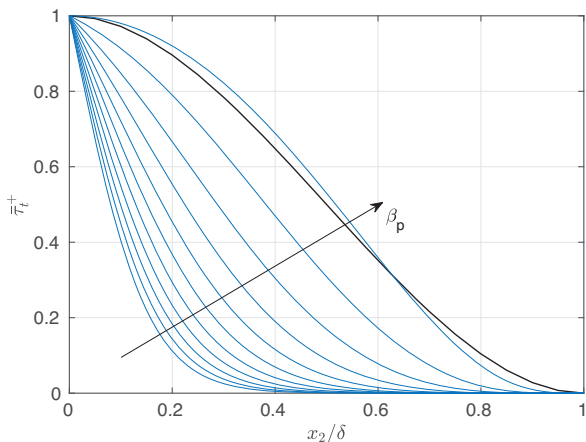


Figure 2. Profiles of $\bar{\tau}_t^+$ given by equation (8) for β_P ranging from -10 to 0 (blue) and by equation (7) for $\beta_P = 0$ (black).

A new function is thus proposed for $\beta_P < 0$:

$$\bar{\tau}_t^+ \simeq 1 + \tanh\left(\frac{\beta_P \zeta_2 - 3\zeta_2^2}{1 - \zeta_2^5 + 0.5}\right), \quad (8)$$

which respects the previously discussed constraints. The constant 0.5 is added to the denominator to prevent $\bar{\tau}_t^+$ from reaching null values too early, as this would lead to velocity profiles reaching a plateau at lower x_2^+ .

As illustrated in Figure 2, equations (7) and (8) give similar profiles for $\beta_P = 0$, but equation (8) gives positive values even for strong favourable gradients, which is necessary for the computation of the velocity profiles. In the remainder of the study, equation (8) is thus taken for all favourable pressure gradients.

3 Validation of the mean velocity modelling

To validate this numerical procedure, the model is benchmarked against experimental data at various Reynolds numbers and under different pressure gradient conditions. First, zero-pressure gradient (zpg) conditions are reported in Figure 3, where the modelled velocity profiles are compared to data from Österlund [28] at three values of Re^+ . The values of x_2^+ at the edge of the boundary layer are naturally recovered since they are equal to their corresponding Re^+ . The viscous sublayer, logarithmic region and outer region are all well matched by the modelled profiles at the three Reynolds numbers.

The modelled profiles are then tested for relatively strong adverse pressure gradients (apg) conditions ($\beta_P \sim 4 - 5$), using data from Prigent, Salze, and Bailly [29], Salze et al. [30] (Fig. 4). Measurements were conducted on a flat surface and the pressure gradient was created by the inclination of the wind tunnel's ceiling. Apart from a 4% over-estimation of the outer velocity at $Re^+ = 2.1 \times 10^3$, the profiles are well matched in the logarithmic and outer regions. Data points are not available in the viscous sublayer, but profiles should mainly be affected by the pressure gradient towards the outer region.

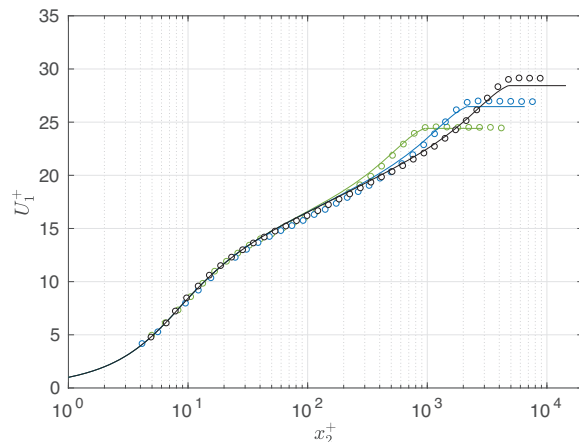


Figure 3. Mean velocity profiles under zero-pressure gradient conditions: comparison between experimental data from Österlund [28] (circles) and model (solid line) at $Re^+ = 9.7 \times 10^2$ (green), $Re^+ = 2.1 \times 10^3$ (blue) and $Re^+ = 4.8 \times 10^3$ (black).

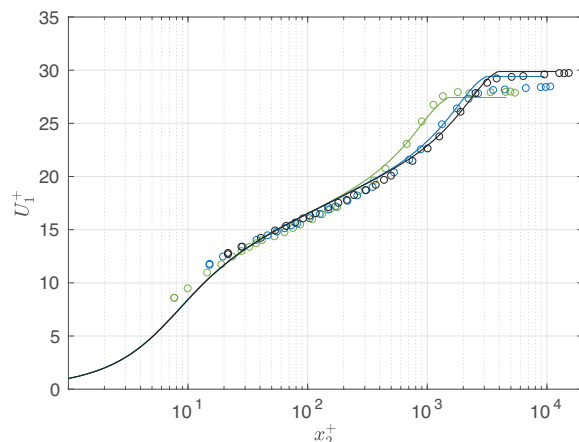


Figure 4. Mean velocity profiles under adverse pressure gradient conditions: comparison between experimental data from Prigent, Salze, and Bailly [29] (circles) and model (solid line) at $Re^+ = 1.5 \times 10^3$ and $\beta_P = 4.3$ (green), $Re^+ = 3.2 \times 10^3$ and $\beta_P = 4.5$ (blue), and $Re^+ = 4.0 \times 10^3$ and $\beta_P = 4.3$ (black).

Figure 5 shows the mean velocity profiles for mild and strong favourable pressure gradients (fpg), comparing the modelled one to the numerical simulations of Cohen and Gloerfelt [5] and experimental data from Prigent, Salze, and Bailly [29]. In the inner region, the numerical profiles rapidly depart from the $U_1^+ = x_2^+$ law and are therefore lower than the modelled ones. Although the log region is short due to the low value of the Reynolds number, the profiles collapse well in this region. In the outer region, the modelled profiles are slightly higher than the numerical data, by 2%. A good match is also observed with the experimental data, at higher Reynolds number. The main limitation in that latter case is the underestimation of the boundary layer thickness, that one can see since the outer plateau is reached earlier. Nonetheless, the modelled profiles are satisfactory in those conditions too.

Overall, this approach offers a reliable mean to model the mean velocity profiles with strong adverse or favourable conditions.

4 Practical considerations on velocity spectra

As discussed in the introduction, recent studies have highlighted the importance of accounting for anisotropy when using velocity data to compute or model the wall pressure spectra. To keep the approach as simple as possible, the present study does not use data to inform models and therefore does not account for local anisotropy. The von Kármán model for the velocity spectra will be used hereafter, to keep with previous studies. It is true that other models such as Liepman or based on the rapid distortion theory could bring some slight improvement [26] but it already gives a good approximation of the velocity correlations [12, 26]. Note that stretching factors could be readily introduced and the same method could be carried out with another model.

Using a von Kármán model, the velocity spectral tensor is written as

$$\phi_{ij}(k) = \frac{E(k)}{4\pi k^4} (\delta_{ij}k - k_i k_j),$$

where the turbulent kinetic energy spectrum is given by

$$E(k) = \frac{55\alpha_1}{9} u'^2 L_e \frac{(kL_e)^4}{(1 + (kL_e)^2)^{17/6}}, \quad (9)$$

with

$$\alpha_1 = \frac{\Gamma(5/6)}{\sqrt{\pi}\Gamma(1/3)}.$$

For the implementation of the tno-Blake formulation, one needs the corresponding 2D cross spectra which is obtained by inverse Fourier transforming along k_2 . This has already been derived by Wilson [31], for a generalised von Kármán spectrum which leads to

$$\begin{aligned} \Phi_{pp}^{mo}(\omega) &= 8\rho^2 \frac{55\alpha_1}{81} \frac{\Gamma(\frac{5}{6})}{\Gamma(\frac{17}{6})} \int_0^\infty \left(\frac{dU_1}{dx_2}\right)^2 \frac{k_c^2 L_e^5}{U_c} u_2'^2 \\ &\times \int_{-\infty}^\infty \left(1 + \frac{k_c^2 + k_3^2}{k_e^2}\right)^{-\frac{7}{3}} e^{-2\sqrt{k_c^2 + k_3^2}x_2} dk_3 dx_2, \end{aligned} \quad (10)$$

where normalisation has been taken to be in line with equation (9). Note that in deriving this equation, the vertical integral scale L_2 was set to the integral correlation length of the vertical velocity fluctuations Λ_{22}^2 . Under the assumption of isotropic turbulence, Λ_{22}^2 is equal to the longitudinal integral length scale Λ , and as reminded by Grasso et al. [11], Jaiswal et al. [12], the correlation length L_e in the generalised von Kármán spectrum is linked to Λ by:

$$\Lambda = \sqrt{\pi} \frac{\Gamma(5/6)}{\Gamma(1/3)} L_e. \quad (11)$$

With the model from Lysak [15], the formulation is

$$\begin{aligned} \Phi_{pp}^{Lysk}(\omega) &\simeq 2\rho^2 \frac{55\alpha_1}{9} \int_0^\infty \left(\frac{dU_1}{dx_2}\right)^2 \frac{k_c^2 L_e^5}{U_1} u_2'^2 \\ &\times \int_{-\infty}^\infty \left(1 + \frac{k_c^2 + k_3^2}{k_e^2}\right)^{-17/6} e^{-2\sqrt{k_c^2 + k_3^2}x_2} dk_3 dx_2. \end{aligned} \quad (12)$$

Finally, both formulations require the correlation length scale $L_e = 1/k_e$ and the vertical velocity fluctuations $\overline{u_2'^2}$. Following from Aupoix [32] and Morilhat et al. [16], one can take $\overline{u_2'^2} \simeq 1.3\overline{u_1' u_2'}$, although this relation is mainly valid in the logarithmic region. Using the previously discussed mixing length model one has, as a function of x_2 :

$$\overline{u_2'^2} \simeq 1.3 l_m \frac{dU_1}{dx_2}. \quad (13)$$

The characteristic wavenumber k_e is linked to the mixing length by

$$k_e = \frac{C_{k_e}}{l_m} \quad \text{with} \quad C_{k_e} = \frac{\sqrt{\pi}}{2} \frac{\Gamma(5/6)}{\Gamma(1/3)}. \quad (14)$$

5 Results

5.1 Frequency spectra

The frequency spectra computed with equations (10) and (12) are shown in Figure 6, along with a series of experimental data for comparison in zero-pressure gradient conditions (zpg). Spectra and frequencies are normalised with the inner scales as $\omega^+ = \omega \times v/\tau_w^2$ and $S_{pp}^+ = S_{pp} \times u_\tau^2/(\tau_w^2 v)$. The modelled spectra are based on the Re^+ values of measurements from Prigent, Salze, and Bailly [29] which are displayed in blue. Other experimental measurements taken from the literature at matching Re_θ are shown in black symbols. Finally, the Goody model is also given, based on the data from Prigent, Salze, and Bailly [29]. Although the levels of the tno-based and Lysak-based models differ over the whole range of frequencies, their shapes and trends are the same. At low frequencies, the models tend to the expected ω^2 power law, initially derived for zero Mach numbers by application of the Kraichnan–Phillipps theorem and under the assumption of frozen turbulence, but which was shown to hold at finite Mach for small non-zero frequencies, see Bull [2] for more details. At high frequencies, they both decay faster than the ω^{-5} power law [2], included in the Goody model. However, one notices that most of the collected experimental data also decay faster than -5 and the modelled spectra are within the bounds of the reported data. Bradshaw [33] argued that the overlap range, from around $\omega^+ = 4 \times 10^{-2}$ to $\omega^+ = 5 \times 10^{-1}$ here, was mainly influenced by

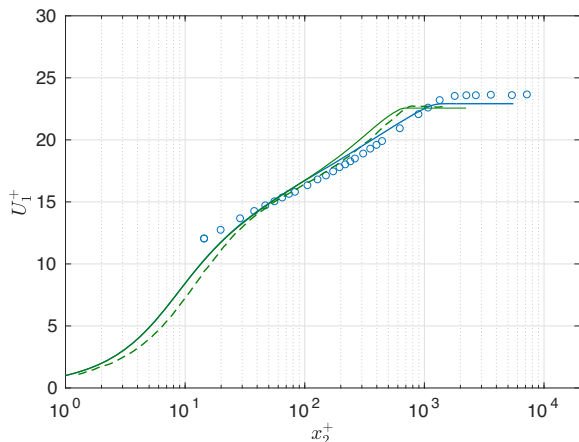
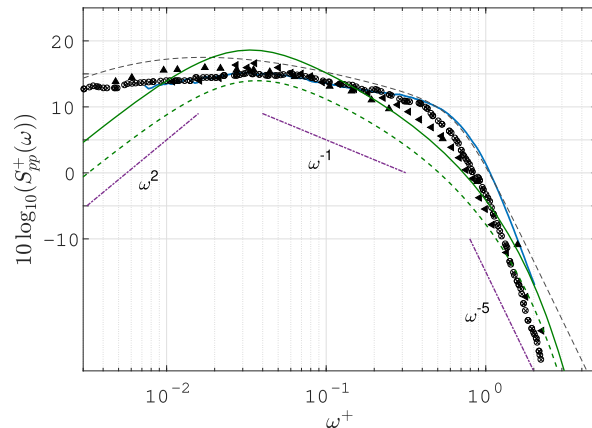


Figure 5. Mean velocity profiles under favourable pressure gradient conditions: comparison between numerical data from Cohen and Gloerfelt [5] (dash) and model (solid line) at $Re^+ = 745$ and $\beta_P = -1.23$ (green), and between experimental data (circles) and model (solid line) at $Re^+ = 1850$ and $\beta_P = -6.0$ (blue).

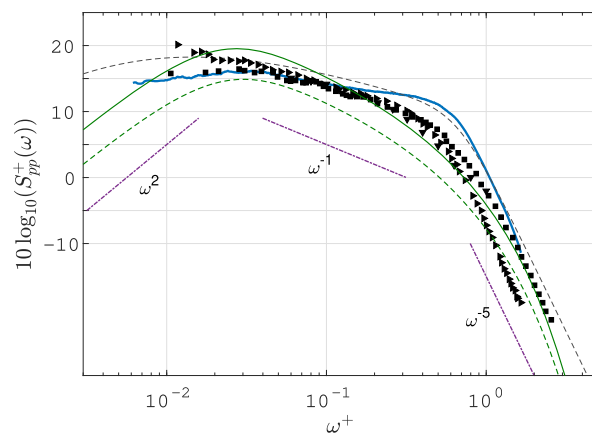
the logarithmic region of the boundary layer, and that dimensional analysis lead to a k_1^{-1} , or conversely ω^{-1} , dependency [2, 33]. Meyers, Forest, and Devenport [34] pointed out that the decay rate is often measured around -0.7 instead of -1 , except at very high Reynolds numbers, in some atmospheric flows for instance. This indeed corresponds to the reported data. With the current modelled spectra, the decay rate does not change with Reynolds number, only the extent of the overlap range does, so that for high Reynolds numbers (tested for $Re^+ = 10^2 - 10^5$ but not illustrated for brevity) the ω^{-1} decay rate is much clearer, while the high frequency part of the spectra remains unchanged. With the Reynolds numbers displayed in Figure 6, the modelled spectra tend to such a decay only for frequencies just below $\omega^+ = 10^{-1}$, and rapidly deviate from it as frequency increases whereas experimental data or Goody model follow their decay rate until around $\omega^+ = 5 \times 10^{-1}$. This is noteworthy since the velocity profiles display the same logarithmic region.

In terms of level, the discrepancies between the measured data and the Lysak-based spectra are of the same order as for the Goody model, albeit stronger towards higher frequencies. The tno-based spectra are below the data, except for the highest frequencies, and therefore lead to stronger discrepancies. Overall, although the overlap region is smaller than for experimental data, the three frequency regions are observed and the levels of the spectra are estimated within 5 dB for most of the frequency range.

The effect of a pressure gradient on the frequency spectra is illustrated in Figure 7, where experimental data from [29] and modelled spectra are displayed for two Reynolds number comparing favourable (fpg), zero- (zpg) and adverse (apg) pressure gradient conditions, with parameters listed in Table 1. For a given Reynolds number, the experimental data clearly show that going from favourable to adverse conditions increases the level of the spectra in



(a) $Re_\theta \sim 5.1 \times 10^3$



(b) $Re_\theta \sim 7.5 \times 10^3$

Figure 6. Comparison of modelled spectra with previous studies at similar Re_θ . Data from from: — Prigent, Salze, and Bailly [29], \oplus Schewe [35], \otimes and \diamond Farabee and Casarella [36], \blacktriangleleft and \blacksquare Gravante et al. [37], \blacktriangle Olivero-Bally et al. [38], \blacktriangleright Goody and Simpson [39], \blacktriangledown Bull and Thomas [40], \odot Blake [41] and \bullet Goody and Simpson [39]. Models, matching conditions from Prigent, Salze, and Bailly [29]: - - - Goody model, — extended Lysak, - - - extended tno. - · - · power laws added for reference.

particular at low frequency where the increase from zpg to apg is close to 5 dB around $\omega^+ = 2 - 3 \times 10^{-2}$. While the discrepancies, in levels and decay rates, between modelled and measured spectra have been discussed before, this low frequency increase with the pressure gradient is clearly rendered in the modelled ones. Under greater pressure gradients, the mean velocity profiles are increased in the outer region, generally associated with large structures and low frequencies, it is thus not surprising that the main effect should be an increased content in the low frequency region. It is nonetheless interesting to note that although this is not clear for fpg, both the amplitude of the increase and the frequency of the maxima are correctly rendered for the zpg and apg cases. Contrarily, the modelled spectra collapse at high frequencies, due to the structure of the model itself. As ω increases, so does k_c and hence by

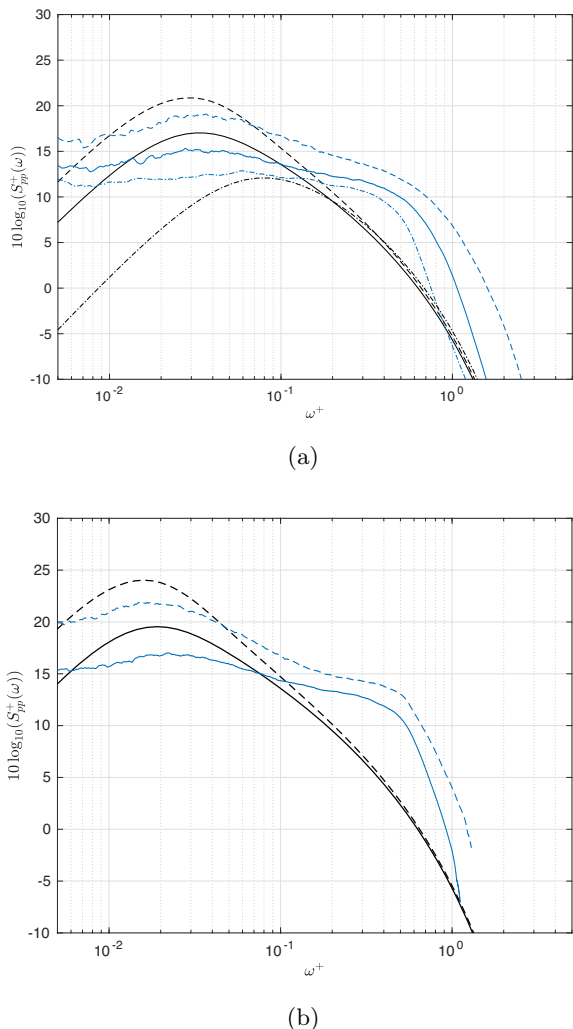


Figure 7. Comparison of modelled (black) and measured (blue) spectra at (a) $Re^+ = 2000$ and (b) $Re^+ = 4000$ for apg (dashed), zpg (solid) and fpg (dash-dotted) conditions. See parameters in Table 1.

Table 1. Parameters of the experimental data [29] used in Figure 7.

	Re^+	β_P
zpg	2.1×10^3	–
	4.0×10^3	–
apg	2.0×10^3	3.7
	4.0×10^3	4.3
fpg	1.9×10^3	–6.0

construction from the exponential in equations (10) and (12), the contribution from small x_2 becomes predominant, where no variation is rendered in the velocity profiles. One should note that variation between spectra measured for different pressure gradients cannot be explained by uncertainties in the measurement of the friction velocity, which has been determined through various methods, see Prigent

et al. [29]. A different scaling could therefore be sought after for such a collapse.

The discrepancies between modelled and measured spectra highlight the limitations of the current approach, which despite correctly rendering the velocity profiles, still misses features of the frequency spectra. So far, ϕ_m has been set under the assumption of frozen turbulence. While this is a classical hypothesis, a more realistic formulation would change the dispersion relation and hence directly affect the spectra. For instance, a correlation function not only accounting for the convection by the mean flow but also for an exponentially decaying envelop in the stream-wise direction could be used in the formulation, but it would require to carry on the derivations without expressing it in a Fourier space. This is an open question that could be addressed in future studies.

5.2 k – ω spectra

The wavenumber–frequency formulation of the spectra models, given in equations (2) and (3) also gives information on the spatial structure of the pressure fluctuations. For a given frequency, ω_0 , a $k_1 - k_3$ representation of $\Phi_{pp}(k_1, k_3, \omega_0)$ can be obtained by computing the integral along x_2 in each model. In the following, this is simplified by taking $\phi_m(\omega, \mathbf{k}) = \delta(\omega - U_1 k_1)$ for both models, that is assuming the frozen turbulence hypothesis holds. While this is a common assumption, it has strong implications that one should keep in mind. For a given frequency, ω_0 , each value of k_1 leads to a single value of U_1 satisfying the dispersion relation. The velocity profiles being strictly monotonous, this in turns implies that only one position in the boundary layer contributes to the spectrum for this particular set of ω_0 and k_1 , which verifies $U_1(x_2) = \omega_0/k_1$. In practice, all relevant x_2 -dependant terms are taken at this position and if ω_0/k_1 is out of the bounds of the velocity profile, the associated value is set to zero in the spectrum. One understands it cannot be physically correct; however, given that the derivation of the tno-Blake formulation assumes a decorrelation of velocity fluctuations across the x_2 direction, such a simplification of the dispersion relation is not out of line.

Figure 8 shows the contour levels of the convective ridge, normalised by its maximum, for three values of the pressure gradient at $Re^+ = 2600$ and at the fixed frequency $\omega_0^+ = 0.05$, computed with the Lysak formulation equation (12) and a von Kármán spectrum for ϕ_{22} . The low frequency is chosen to fall in the region where most of the difference is expected. The reader should note that, for ease of visualisation, the axes are not orthonormal and the ridges are therefore more elongated along k_3 than they appear. In the zpg case, the contours exhibit some expected features: they are elongated in the k_3 direction and asymmetric along k_1 with a steeper decay towards low wavenumbers. The effect of pressure gradients is clear, with contours that are more elongated in fpg and more compact in apg, with an additional distortion stretching the ridge towards low wavenumbers. In turn, the aspect ratio of those ridges are clearly increased from apg to zpg then fpg, which had been reported in both experimental [29] and numerical [5] data.

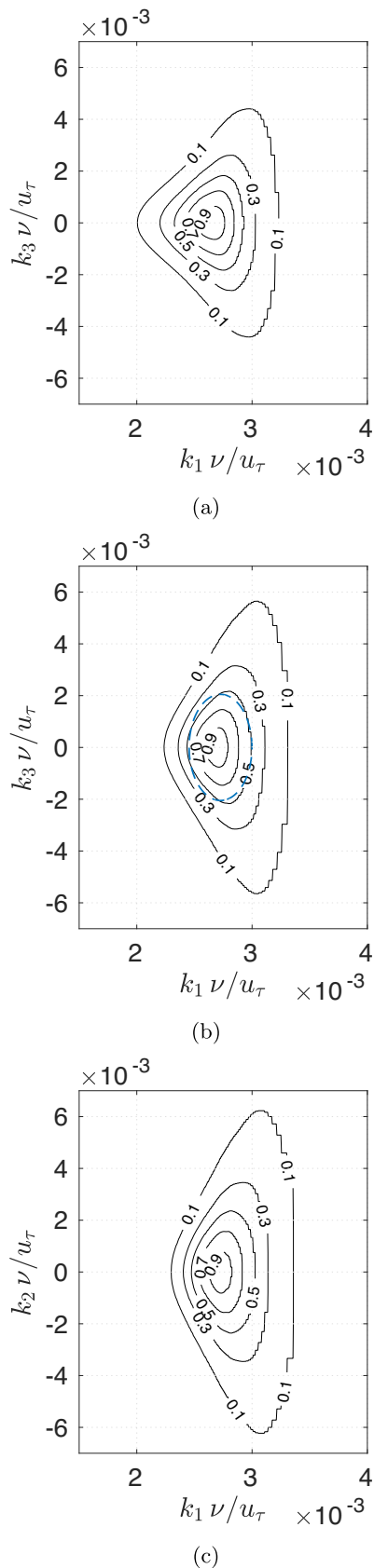
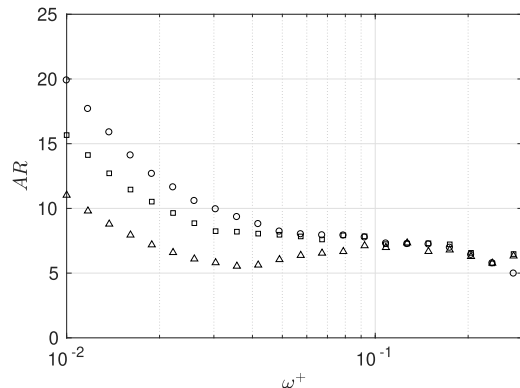
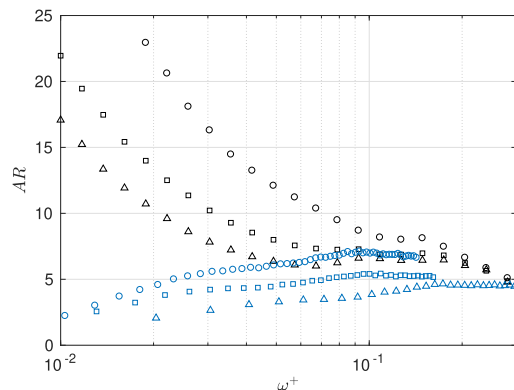


Figure 8. Modelled spectra at $\omega^+ = 0.05$, $\text{Re}^+ = 2600$ and (a) $\beta_p = 10$ (apg), (b) $\beta_p = 0$ (zpg) and (c) $\beta_p = -2$ (fpg). An ellipse (dashed) is fitted to the half-level contour in (b).



(a) $\text{Re}^+ = 2600$ for $\beta_p = 10$, $\beta_p = 0$ and $\beta_p = -2$



(b) apg $\text{Re}^+ = 1.5 \times 10^3$ & $\beta_p = 4.3$; zpg $\text{Re}^+ = 1.3 \times 10^3$ & $\beta_p = 0$ and fpg $\text{Re}^+ = 1.8 \times 10^3$ & $\beta_p = -6$

Figure 9. Aspect ratio of the half level contour for apg (Δ), zpg (\square) and fpg (\circ) conditions.

The aspect ratio of the half-level contour is computed for a wide range of frequencies for flow conditions from Figure 8 and reported in Figure 9a. This computation is automatized by fitting an ellipse to the half level contour, as illustrated in Figure 8(b). Although the convective ridge is not expected to be truly elliptical, this gives a fair estimate of the aspect ratio and removes the risk of accounting for spurious points when processing experimental data. For low frequencies, below $\omega^+ = 10^{-1}$, the difference is striking with the aspect ratio in favourable conditions up to twice that of adverse conditions. At frequencies higher than $\omega^+ = 10^{-1}$, no clear difference between the pressure gradients can be observed, which goes along the idea that pressure gradients mostly affect the outer part of the mean velocity profiles.

Figure 9b shows the aspect ratio computed from experimental data [29] for favourable, zero- and adverse pressure gradients. Modelled aspect ratios are also displayed for matching conditions. The model clearly overestimates the aspect ratio for all cases and particularly so at low frequencies. However, the increase from adverse to favourable conditions is indeed observed in both the experimental and modelled data. This variation tends to weaken at higher frequencies, which could be expected since the variations in the frequency spectra were more significant at low

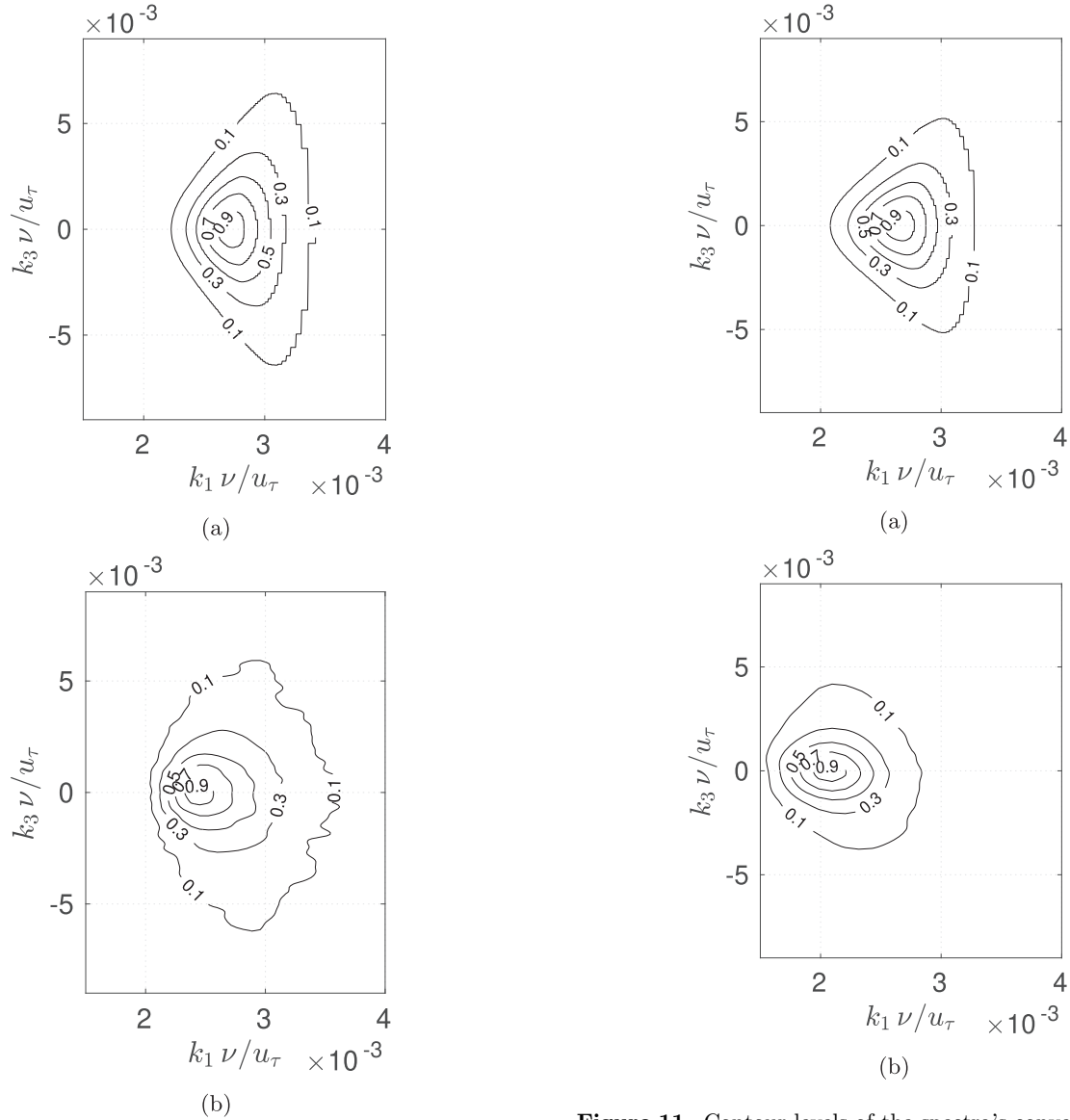


Figure 10. Contour levels of the spectra's convective ridge for (a) modelled and (b) experimental data at $\omega^+ = 0.05$, $\text{Re}^+ = 1.3 \times 10^3$ and $\beta_P = 0$.

frequencies. While these trends are always found, the exact value of the aspect ratio depends on which level is taken to compute it. The half level contour has been chosen here, but a similar analysis could be conducted with another level.

A more detailed comparison between experimental data [29] and modelled spectra is provided in Figures 10–12. For the zpg case, the value of $k_1 \nu / u_\tau$ corresponding to the maximum of the convective ridge is slightly over-estimated by the model, 2.7 instead of 2.4. This value strongly depends on the dispersion relation used in the computation of the spectrum since it prescribes the x_2 -dependent quantities taken into account. For instance, introducing a coefficient smaller than one in the previous definition of $U_1(x_2)$ would shift the ridge towards smaller k_1 . With these words of caution, the ridge maximum is satisfactorily predicted by the model. In addition to the previously discussed aspect

Figure 11. Contour levels of the spectra's convective ridge for (a) modelled and (b) experimental data at $\omega^+ = 0.05$, $\text{Re}^+ = 1.5 \times 10^3$ and $\beta_P = 4.3$.

ratio, the asymmetry of the ridge is clearly visible in both modelled and measured spectra with a faster decay towards low wavenumbers. However, the shape of the contours is exaggeratedly flattened on their high wavenumber side in the modelled spectra. The same observations can be made for the apg case, although the discrepancy in $k_1 \nu / u_\tau$ for the maximum of the ridge is stronger than for zpg. For fpg conditions, the experimental data exhibit a slight unexpected twist and the model also flattens the high wavenumber side. Finally, the shape of the modelled spectra exhibits a protuberance that points towards low wavenumbers, particularly visible for the apg case. Looking back at equation (3), the observed discrepancies can have several causes. First, and given the good match between measured and modelled mean velocity profiles, the mean shear term is unlikely a main contribution to the discrepancies. Contour

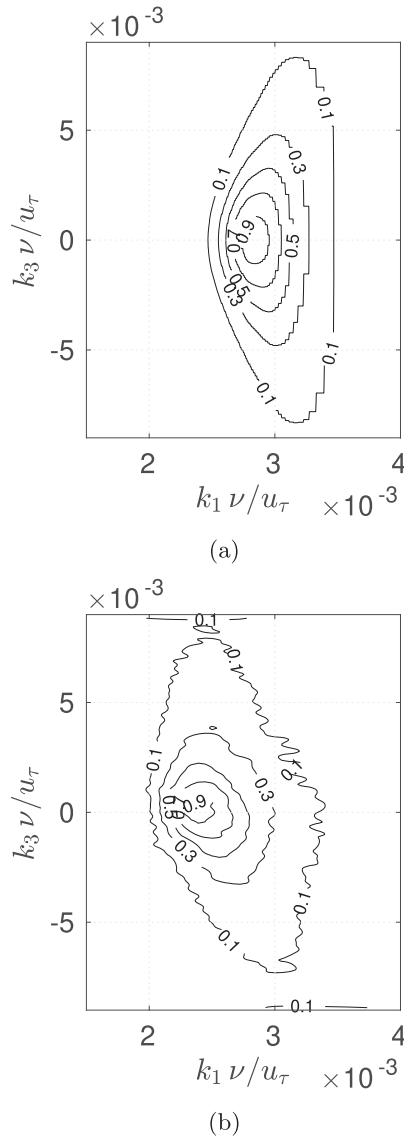


Figure 12. Contour levels of the spectra’s convective ridge for (a) modelled and (b) experimental data at $\omega^+ = 0.05$, $\text{Re}^+ = 1.8 \times 10^3$ and $\beta_P = -6$.

plots have also been computed with the tno-Blake approach (eq. (2)) and three orders of the generalised von Kármán model for the velocity fluctuations ϕ_{22} : the standard von Kármán one, Liepman’s one and the rapid distortion theory model. The output is not shown for brevity, but the changes are marginal. Assumptions made regarding homogeneity and isotropy of the flow could be contributing factors to this. However, as discussed in the introduction, most of the existing studies rely on experimental or numerical data to tune the models. These limitations might be a drawback one has to accept in order to keep the approach as simple as possible and to rely on only two non-dimensional parameters. It is fair to say that ϕ_m most likely plays a role, as discussed before. Finally, the structure of the tno-Blake or Lysak formulations, and their derivation leading to the fractional and exponential terms in the integrand must structure the shape of the model. Indeed, the product of

these two terms gives contours pointing towards low wavenumbers that are weighting in the integral.

Despite the observed discrepancies, the modelled spectra exhibit the expected characteristics and show the trends of the effect of pressure gradients, this can provide useful qualitative information. In addition, the availability of two-dimensional experimental data provides a useful insight that allows the discussions of these discrepancies before they are hidden out by the successive integrations leading to the frequency spectra.

6 Concluding remarks

The approach followed in this paper uses a model of the shear stress across the boundary layer to enable, through a mixing length model, the computation of velocity profiles and relevant turbulent quantities that are inputs to existing wall pressure spectra models. The inclusion of the mean pressure gradient in the shear stress model, and in particular the new formulation proposed for favourable conditions, offers a new semi-analytical means to study its effects on wall pressure spectra.

Despite the simplicity of its formulation, this approach has proven useful in estimating the levels of the frequency spectra and observing the trends of how mean pressure gradients effect on them. The three typical region of such spectra are recovered, although the overlap region is shorter and exhibits a -1 power law decay and not the -0.7 one usually expected for moderate Reynolds numbers. Further investigation into the formulation of ϕ_m , setting the dispersion relation of the frequency dependence, could help better capture the features of such spectra.

Typical features of the convective ridge (i.e. asymmetry between low and high wavenumber sides, elongation along the transverse direction) are found in the modelled wavenumber spectra. The availability of two-dimensional experimental data allows for a direct comparison. An increase of the ridge’s aspect ratio from adverse to zero- then favourable pressure gradient is observed, which is qualitatively consistent with experimental and numerical data although the exact values do not match. The shape of the ridge itself displays some discrepancies between modelled and measured spectra, which are used to discuss the effect of various hypotheses and assumptions of the model before they are hidden by integration. Overall, the wavenumber–frequency representation gives a good illustration of the effect of pressure gradients and is useful in discussing the limits of the models.

Finally, the use of a physical equation to be integrated provides robustness and should help avoiding the pitfalls that a bespoke model may encounter when used outside of its range of optimisation. Be it at an advance stage assessment or for the investigation of various parameters’ effect, this approach can therefore prove useful for many applications.

Conflict of interest

The authors declare no conflict of interest.

Acknowledgments

The present study has been conducted as part of the project BRIO, funded by the Auvergne-Rhône-Alpes region (AURA – 909 92 204181). This work was performed within the framework of the Labex CeLyA of the Université de Lyon, within the programme ‘Investissements d’Avenir’ (ANR-10-LABX-0060/ANR-16-IDEX-0005) operated by the French National Research Agency.

References

1. W.W. Willmarth: Pressure fluctuations beneath turbulent boundary layers. *Annual Review of Fluid Mechanics* 7, 1 (1975) 13–36.
2. M.K. Bull: Wall-pressure fluctuations beneath turbulent boundary layers: Some reflections on forty years of research. *Journal of Sound and Vibration* 190, 3 (1996) 299–315.
3. D. Juvé, S.L. Prigent, E. Salze, P. Souchotte, C. Bailly: Opening lectures–wall-pressure wavenumber–frequency spectra: Experimental challenges and recent advances, in *International Conference on Flow Induced Noise and Vibration Issues and Aspects*, Springer, 2019, pp. 1–23.
4. M. Slama, C. Leblond, P. Sagaut: A kriging-based elliptic extended anisotropic model for the turbulent boundary layer wall pressure spectrum. *Journal of Fluid Mechanics* 840 (2018) 25–55.
5. E. Cohen, X. Gloerfelt: Influence of pressure gradients on wall pressure beneath a turbulent boundary layer. *Journal of Fluid Mechanics* 838 (2018) 715–758.
6. D.J. Fritsch, V. Vishwanathan, K. Todd Lowe, W.J. Devenport: Fluctuating pressure beneath smooth wall boundary layers in nonequilibrium pressure gradients. *AIAA Journal* (2022) 1–19.
7. M. Goody: Empirical spectral model of surface pressure fluctuations. *AIAA Journal* 42, 9 (2004) 1788–1794.
8. Y. Rozenberg, G. Robert, S. Moreau: Wall-pressure spectral model including the adverse pressure gradient effects. *AIAA Journal* 50, 10 (2012) 2168–2179.
9. S. Lee: Empirical wall-pressure spectral modeling for zero and adverse pressure gradient flows. *AIAA Journal* 56, 5 (2018) 1818–1829.
10. R.H. Kraichnan: Pressure fluctuations in turbulent flow over a flat plate. *The Journal of the Acoustical Society of America* 28, 3 (1956) 378–390.
11. G. Grasso, P. Jaiswal, H. Wu, S. Moreau, M. Roger: Analytical models of the wall-pressure spectrum under a turbulent boundary layer with adverse pressure gradient. *Journal of Fluid Mechanics* 877 (2019) 1007–1062.
12. P. Jaiswal, S. Moreau, F. Avallone, D. Ragni, S. Pröbsting: On the use of two-point velocity correlation in wall-pressure models for turbulent flow past a trailing edge under adverse pressure gradient. *Physics of Fluids* 32, 10 (2020).
13. W.K. Blake: *Mechanics of flow-induced sound and vibration – General concepts and elementary sources*. Vol. 2, Academic Press Inc., 1986, ISBN 0121035018.
14. R.R. Parchen: Progress report DRAW: A prediction scheme for trailing edge noise based on detailed boundary layer characteristics. TNO Institute of Applied Physics, 1998.
15. P.D. Lysak: Modeling the wall pressure spectrum in turbulent pipe flows. *Journal of Fluids Engineering* 128 (2006) 216–222.
16. S. Morilhat, F. Chedevigne, F. Micheli, F. Simon: Wall-normal velocity correlations in a zero pressure gradient turbulent boundary layer. *Journal of Fluids Engineering* 142, 8 (2020) 081302.
17. F. Bertagnolio, A. Fischer, W.J. Zhu: Tuning of turbulent boundary layer anisotropy for improved surface pressure and trailing-edge noise modeling. *Journal of Sound and Vibration* 333, 3 (2014) 991–1010.
18. D.A. Lynch, W.K. Blake, T.J. Mueller: Turbulence correlation length-scale relationships for the prediction of aeroacoustic response. *AIAA Journal* 43, 6 (2005) 1187–1197.
19. O. Stalnov, P. Chaitanya, P.F. Joseph: Towards a non-empirical trailing edge noise prediction model. *Journal of Sound and Vibration* 372 (2016) 50–68.
20. A. Fischer, F. Bertagnolio, H.A. Madsen: Improvement of two type trailing edge noise models. *European Journal of Mechanics-B/Fluids* 61 (2017) 255–262.
21. C. Bailly, G. Comte-Bellot: *Turbulence*. Springer, 2015.
22. L.C. Thomas, S.M.F. Hasani: Supplementary boundary-layer approximations for turbulent flow. *Journal of Fluids Engineering* 111 (1989) 420–427.
23. F.M. White: *Viscous fluid flow*. 3rd ed., McGraw-Hill, New York, 2004.
24. E.R. Van Driest: Turbulent boundary layer in compressible fluids. *Journal of the Aeronautical Sciences* 18, 3 (1951) 145–160.
25. R.A. McD Galbraith, S. Sjolander, M.R. Head: Mixing length in the wall region of turbulent boundary layers. *The Aeronautical Quarterly* 28, 2 (1977) 97–110.
26. P.G. Huang, P. Bradshaw: Law of the wall for turbulent flows in pressure gradients. *AIAA Journal* 33, 4 (1995) 624–632.
27. J. Cousteix, J. Mauss: *Asymptotic analysis and boundary layers*, Springer, Berlin Heidelberg, 2007.
28. J.M. Österlund: Experimental studies of zero pressure-gradient turbulent boundary layer flow. Ph.D. thesis, Royal Institute of Technology, 1999.
29. S.L. Prigent, É. Salze, C. Bailly: Wall pressure spectra and convection: Two-dimensional analysis under mean pressure gradients. *AIAA Journal* 60, 6 (2022) 3707–3723.
30. É. Salze, C. Bailly, O. Marsden, E. Jondeau, D. Juvé: An experimental characterisation of wall pressure wavevector-frequency spectra in the presence of pressure gradients, in 20th AIAA/CEAS Aeroacoustics Conference, Atlanta, GA, USA, 16-20 June 2014, 2909 p.
31. D.K. Wilson: Three-dimensional correlation and spectral functions for turbulent velocities in homogeneous and surface-blocked boundary layers. Technical report, Army Research Lab, Adelphi, MD, 1997.
32. B. Aupoix: Extension of lysak’s approach to evaluate the wall pressure spectrum for boundary layer flows. *Flow, Turbulence and Combustion* 94, 1 (2015) 63–78.
33. P. Bradshaw: “Inactive” motion and pressure fluctuations in turbulent boundary layers. *Journal of Fluid Mechanics* 30, 2 (1967) 241–258.
34. T. Meyers, J.B. Forest, W.J. Devenport: The wall-pressure spectrum of high-reynolds-number turbulent boundary-layer flows over rough surfaces. *Journal of Fluid Mechanics* 768 (2015) 261–293.
35. G. Schewe: On the structure and resolution of wall-pressure fluctuations associated with turbulent boundary-layer flow. *Journal of Fluid Mechanics* 134 (1983) 311–328.
36. T.M. Farabee, M.J. Casarella: Spectral features of wall pressure fluctuations beneath turbulent boundary layers. *Physics of Fluids A: Fluid Dynamics* 3, 10 (1991) 2410–2420.
37. S.P. Gravante, A.M. Naguib, C.E. Wark, H.M. Nagib: Characterization of the pressure fluctuations under a fully developed turbulent boundary layer. *AIAA Journal* 36, 10 (1998) 1808–1816.

38. P. Olivero-Bally, B.E. Forestier, E. Focquenoy, P. Olivero, et al.: Wall-pressure fluctuations in natural and manipulated turbulent boundary layers in air and water. ASME-Publications-Fed 168 (1993) 63.
39. M.C. Goody, R.L. Simpson: Surface pressure fluctuations beneath two-and three-dimensional turbulent boundary layers. AIAA Journal 38, 10 (2000) 1822–1831.
40. M.K. Bull, A.S.W. Thomas: High frequency wall-pressure fluctuations in turbulent boundary layers. The Physics of Fluids 19, 4 (1976) 597–599.
41. W.K. Blake: Turbulent boundary-layer wall-pressure fluctuations on smooth and rough walls. Journal of Fluid Mechanics 44, 4 (1970) 637–660.

Cite this article as: Prigent SL. & Bailly C. 2022. From shear stress to wall pressure spectra: a semi-analytical approach to account for mean pressure gradients in turbulent boundary layers. Acta Acustica, 6, 43.